# 3D-Sensor Assisted Robotic Deburring of Aerospace Engine Bearing Rings

[1]Sven Jörissen, [2]Thorben Schnellhardt, [3]Christian Grohmann, [4]Melanie Schmitt, [3]Marius Bürlein,
[1]Andreas Nüchter
[1]Julius-Maximilians-University Würzburg, Informatics XVII – Robotics, Am Hubland, 97074 Würzburg,
sven.joerissen@uni-wuerzburg.de
[2]Fraunhofer Fraunhofer Institute for Machine Tools and Forming Technology IWU, Pforzheimer Str. 7a,
01189 Dresden, Thorben.Schnellhardt@iwu.fraunhofer.de
[3]Toolcraft AG, Handelsstraße 1, 91166 Georgensgmünd
[4]Schaeffler Aerospace Germany GmbH & Co. KG, Georg-Schäfer-Straße 30, 97421 Schweinfurt

**Abstract**: Aerospace manufacturing faces strict quality requirements and high part variety, often produced in low quantities. While conventional automation improves quality and efficiency, it is impractical in high-mix low-volume settings due to high planning overhead. Hence, deburring, requiring adaptive processing for workpiece tolerances, remains largely manual. This paper presents a novel method for adaptive robotic deburring of aerospace engine bearing rings manufactured in high-mix low-volume contexts. The proposed method uses two 3D sensors to reduce cycle times while meeting quality requirements. A 3D camera with a large measurement range locates the workpiece, while a second, high-resolution sensor scans the burr areas. Pairwise registration refines the scans for improved global consistency. An indirect RANSAC-based method detects adjacent edge surfaces and reconstructs the edge by computing surface intersections. Conventional offline planning strategies generate the adaptive robot path. The processing pipeline was implemented on a calibrated CNC robot with secondary encoders and yielded promising results in first experiments. The method succeeded where paths based on the nominal CAD model failed. It eliminated measurement and path planning effort. However, it can’t handle freeform surfaces and relies heavily on the robot’s accuracy as well as consistent matching.

**Keywords:** deburring, aerospace, robot, 3D-sensor, high-mix/low-volume

## 1 Introduction

Burrs, undesirable material protruding beyond the workpiece, occur during various manufacturing processes. Sharp-edged burrs affect appearance and pose injury risk during processing and end application. Highly stressed components, such as aerospace engine bearing rings, risk stress peaks and crack formation due to sharp edges and inhomogeneous burrs. The FAA mandated over a decade ago that aviation OEMs implement “mechanized edge profiling” to minimize human error in edge shortening production. Automated processes are typically employed for optimal quality and economic efficiency, but they’re impractical for high-mix/low-volume (HM/LV) production due to the high cost of individual work preparation.

Previous research in the field of robotic deburring tried to use 2D camera and Hough transformation for workpiece-specific trajectory generation of straight lines [1]. Kuss et al. [2] used manufacturing tolerances to compare 3D scans to a set of models generated from those tolerances to find the one with the least deviation. Other, semi-automated approaches [3] compare a CAD generated trajectory to manually teached points to adjust for deviations .More recently, Lloyd et al. [4] looked into 2D-laser and stereo camera application for workpiece registration. However, none of the found methods seem to be feasible for both high-mix/low-volume applications and the high accuracy needed for this specific application.

In this work, we developed a robotic deburring cell that minimizes work preparation effort for HM/LV production while meeting aviation sector quality requirements. This approach enhances consistency, reduces costs, and minimizes human error. A robot-guided dual sensor system, comprising two 3D sensors, is employed. One sensor provides low resolution and extensive measurement range for initial workpiece localization, while the other offers high resolution but limited measurement range for precise deburring detection. Adaptive path planning incorporates the actual geometry of the workpiece due to inherent tolerances.

The next section presents our approach to the problem described above. Section 3 presents our experiments and the results, and we conclude the paper with a short discussion and outline for future work.

## 2 Method

In this section we present our method for 3D sensor assisted robotic deburring. Given a CAD model of the workpiece and a selection of sharp edges to be deburred, our goal is to plan deburring tool paths that account for the actual geometry of the workpiece, including shape deviations from the nominal CAD model. Figure 1 outlines the proposed method and its individual steps, which are described in the following subsections.

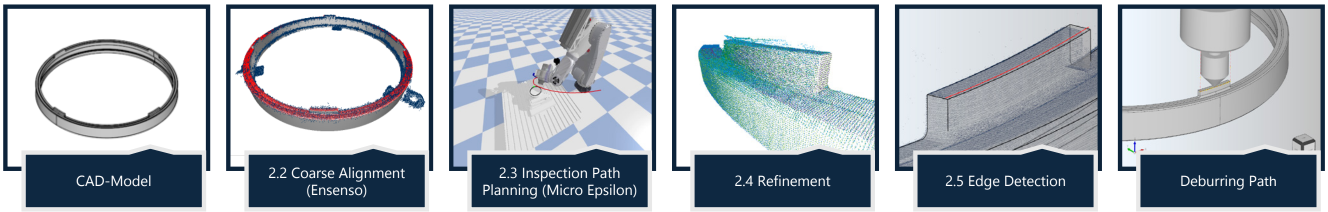

Figure 1: Pipeline for our method of 3D sensor assisted robotic deburring.

### 2.1 Hand-Eye Calibration

First, both 3D sensors need to be calibrated with respect to the robot’s hand. This calibration is called hand-eye calibration and tries to determine the hand-eye transformation $X$ by solving the equation $AX = XB$ with $A$ being a set of transformations between consecutive robot poses and $B$ being the corresponding transformation between consecutive sensor poses relative to a fixed calibration object. Once $X$ is determined, 3D sensor data can easily be converted from the camera’s frame into the robot’s frame. For the Ensenso 3D camera, 20 images of a 200x200 mm calibration pattern with 112 points on a 24 mm grid are captured and then processed using the Ensenso SDK hand-eye calibration tool. For calibration of the 3D snapshot sensor, a custom-built calibration target consisting of four sandblasted bearing balls with a diameter of 8.731 mm, arranged on a three-dimensional structure, is used, depicted in Figure 2, right. As long as at least three of the four balls are detected, the position of the sensor relative to the calibration target is clearly determinable. The data is then processed using Andreff’s method [5].

Given its rotational symmetry and limited defining characteristics, the workpiece in question presents a challenging initial configuration for optical 3D sensors. The relatively small size of the retaining lugs, coupled with the reflective surface, necessitates precise parameterization of both the 3D sensors and the algorithms employed for processing the 3D data.

### 2.2 Coarse Localization

Next, we conduct a coarse localization of the workpiece within the fixture using a 3D sensor with a large measurement range to estimate the pose of the symmetrical workpiece, we combine an iterative closest point (ICP) algorithm with a template matching approach. To obtain an initial estimate of the workpiece’s position, we combine the dimensions derived from the CAD model with the assumption that the workpiece will always occupy the highest point within the working area. Subsequently, a coarsely parameterized ICP is applied to rectify any lateral displacements or tilt errors. To determine the rotation around the z-axis, a template matching algorithm is employed. In this process, the model is rotated 180 degrees around the z-axis in increments of 1 degree. For each increment, the average point-to-plane error between the model and the scan is computed. The increment associated with the lowest average point-to-plane error is subsequently selected, and the model is transformed accordingly. Finally, a finely parameterized ICP is applied to correct any remaining rotational error that is less than 1 degree.

### 2.3 Inspection Path Planning

To acquire data from the regions of interest, we plan and execute a collision-free inspection path using sampling-based motion planning. For each edge selected in the model, we want to find two scan poses for both corners, one with the same robot hand orientation as the deburring process will occur later, and one from the direction of the average normal of all adjacent surfaces. If a scan pose is not reachable by the robot, alternative poses within a 30-degree cone around the original pose are sampled, until a valid pose is found. We use OMPL [6] with BIT* [7] for motion planning and Bullet [8] for collision detection. We then scan the burr areas using a second, high-resolution 3D sensor with a smaller measuring range according to the planned path.

### 2.4 Refinement

ICP is utilized with the one of the poses from the later deburring orientation as a reference, further minimizing the absolute positioning error and getting close to the repeatability of the robot. This improves global consistency and alignment. Outliers (e.g. false detections from the reflective surface) are removed using a statistical outlier removal (SOR) filter and the scans are subsampled based on a voxel grid. Next, the model is registered onto the scans, providing us with the final pose of the workpiece.

### 2.5 Edge Detection

For edge detection, we introduce an indirect RANSAC-based approach that detects the edge adjacent surfaces and reconstructs the edge by computing the surface intersection. First, the registered and cleaned scans are segmented into smooth regions [9] to omit sharp edges and reduce the influence of any remaining outliers. Second, the scans are the cropped to the size of the oriented bounding boxes of the edge adjacent surfaces. We increasing the size of the bounding boxes slightly to account for workpiece tolerances. Within those bounding boxes, RANSAC [10] is used to detect the actual parameters of the edge adjacent surfaces. If multiple surfaces are found, the surface with the smallest parameter deviation from the nominal surface is selected. Next, the adjacent surfaces are intersected to reconstruct the edge.

Finally, we generate the adapted tool path for the reconstructed edge using conventional offline planning strategies for 3-axis wireframe-based deburring. We do not check the tool path for singularities explicitly, as we do not tilt the spindle during the deburring process and the part is clamped in a sufficiently low position to avoid wrist singularities.

## 3 Results

### 3.1 Setup

The robot in question is an Autonox articc.m6-2390-150 kg 6-axis robot with a nominal payload of 150 kg and a working area-reach of 2390 mm. The robot is equipped with Beckhoff motors and a Beckhoff robot controller, and a Hiteco QT-2 25/7 milling spindle with a maximum speed of 16000 rpm. The dual sensor system consists of an Ensenso N36 3D camera with a working distance of 380-770 mm, a measuring area of 565x356 mm and an accuracy of 0.18 mm at 500 mm distance, and a MicroEpsilon SurfaceControl 3500-120 3D snapshot sensor with a working distance of 206±35 mm, a measuring area of 120x75 mm and a z-resolution of 2 µm. Both sensors are mounted next to the milling spindle on a metal frame. This is depicted in Figure 2.

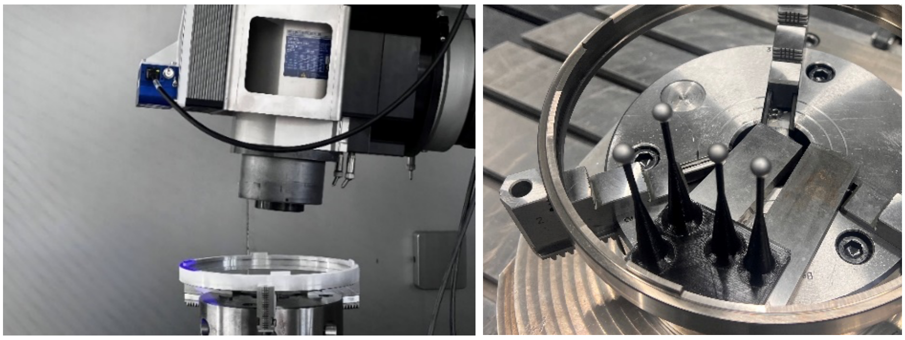

Figure 2: Left: Dual-Sensor-System mounted next to the milling spindle. Right: Calibration structure for the 3D snapshot sensor.

The robot was calibrated using a laser tracker. The absolute accuracy after calibration is 0.42±0.20 mm with a repeatability of 0.07±0.03 mm.

### 3.2 Hand-Eye Calibration

To analyze the result of the hand-eye calibration of the 3D camera, Figure 3, left, shows four top-down scans of the workpiece, taken from four positions, colored in red, green, blue and yellow, respectively. Also, a detailed view of one of the retaining lugs is depicted (middle). Visually, the scans are properly aligned. To support the visual analysis, the point-to-point distances between scans were calculated in pairs. Figure 3, right. shows the histogram of those distances of two overlapping scans. It is evident that 85% of the points have a point-to-point distance of less than 0.7 mm. For a selection of 1721 coplanar points from the scan, all points lie within ±0.5 mm from that plane. Combining the scanner's accuracy with the robot's accuracy and considering the challenging reflective surface of the object, this exactly fits the expectation. For errors greater than 2mm, it is assumed that they are distances between points that were not present in both scans.

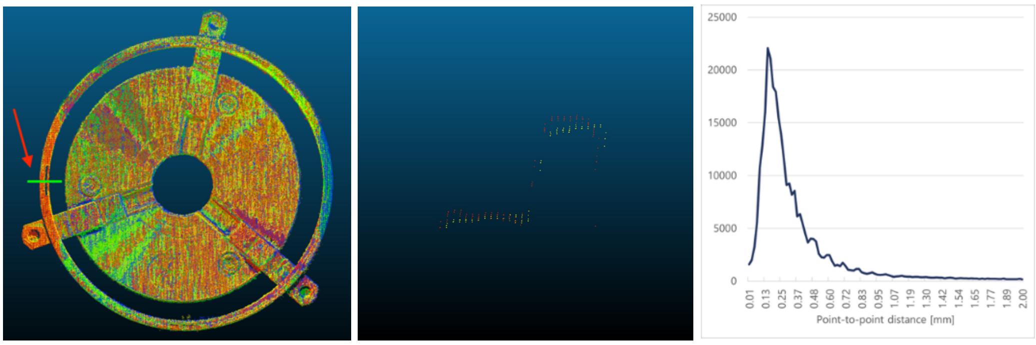

Figure 3: Left: Top view of four overlapping scans from the 3D camera. Center: Cross-sectional view of one retaining lugs as indicated by the red arrow and green line on the left picture. Right: Distribution of the point-to-point distances between two scans of the 3D camera.

Given that the 3D snapshot sensor operates with an accuracy that is two orders of magnitude superior to the accuracy of the robot, it is anticipated that the hand-eye calibration will not adversely affect the overall accuracy of the entire system. To substantiate this assertion, the calibration scans were scrutinized for internal consistency within the calibration pipeline. Initially, for 27 scans of the calibration structure, 83 of 108 bearing balls (27 scans with 4 bearing balls each) were successfully detected. The standard deviation of all fitted sphere radii was calculated to be 0.0093 mm, and the distribution of the calculated radii is illustrated in Figure 4, left. Subsequently, the six distances between all fitted spheres were computed. The standard deviations for all six distances are presented in Figure 4, right. Although these calculations do not directly indicate an accurate hand-eye calibration, they demonstrate the consistency of the scan processing and guarantee that the pose estimation of the scanner relative to the calibration structure is not compromised by noisy and inaccurate data.

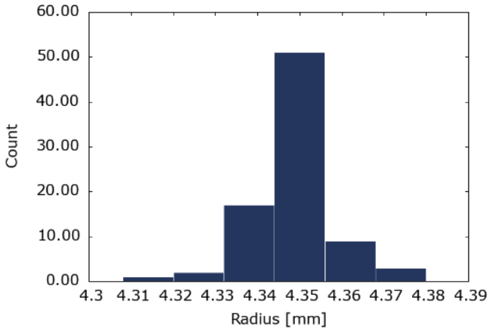

| | |
|---|---|
| Distance 1 | 54.96±0.010 mm |
| Distance 2 | 50.65±0.011 mm |
| Distance 3 | 36.96±0.009 mm |
| Distance 4 | 30.75±0.010 mm |
| Distance 5 | 25.37±0.005 mm |
| Distance 6 | 20.28±0.008 mm |

Figure 4: Left: Distribution of the fitted sphere radii. Right: Calculated distances with standard deviation between spheres.

## 3.3 Coarse Localization

Given the rotational symmetry of the workpiece and the alignment of the x-y plane of the workpiece with the x-y plane of the robot, the previously described pipeline for initial object localization was tested with 8 initial rotations around the z-axis. The final alignment of the scan and model is illustrated in Figure 5, left, while the result of the template matching algorithm for an initial rotation error of 40 ° on the right side is shown on the right. For all tested initial rotation errors, the alignment was successfully computed. To further account for potential errors during workpiece mounting, the alignment was tested for an additional tilting error of up to 10 °, which also resulted in a successful alignment.

## 3.4 Refinement

The refinement pipeline is subsequently applied to the 3D snapshot sensor data. Employing the Iterative Closest Point (ICP) algorithm, any residual positional and rotational errors between scans are minimized and the model is registered onto the scans. For an estimate of the final accuracy, the point-to-point distances between model and scans are calculated. Distances above 0.5 mm are considered noise and therefore omitted. The result for one retaining lug is shown in Figure 6. 90.49% of all points have a point-to-point distance lower than 0.3 mm, which lies within the fabrication tolerances of the respective workpiece.

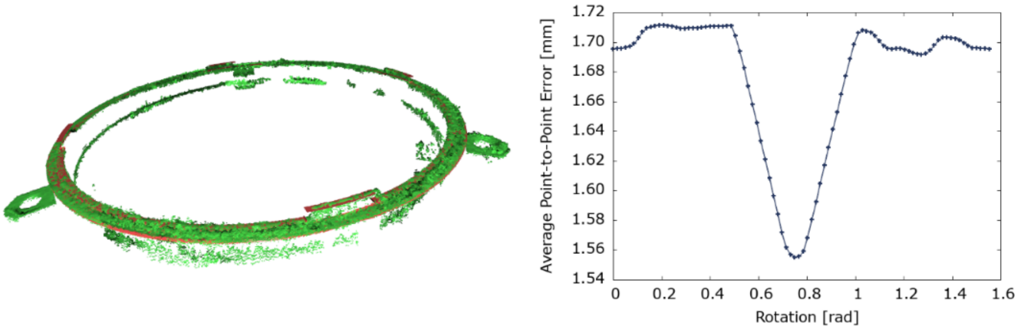

Figure 5: Results of the coarse registration. Left: Scan (green) and registered model (red). Right: Point-to-Point distances of the template matching algorithm for 180 rotations with 1 ° each for an initial rotation error of 40 °.

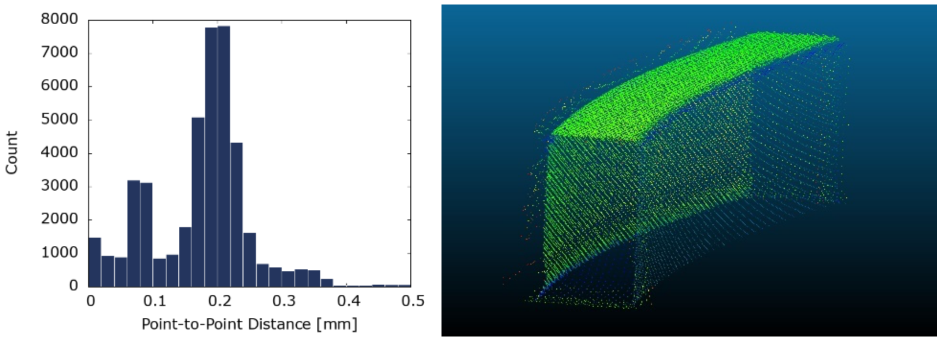

Figure 6: Left: Distribution of the point-to-point distances. Right: Point cloud colored with distances.

## 3.4 Deburring

Figure 7 shows the RANSAC segmentation of the final scan of a retaining lug. A deburring path is then calculated by finding the intersection between adjacent segments as previously described. The result of the deburring is shown in Figure 8. Two experiments were carried out, one on and outside edge and one on the inside. Both tests successfully deburred the edges with the generated trajectory based on the 3D sensor data.

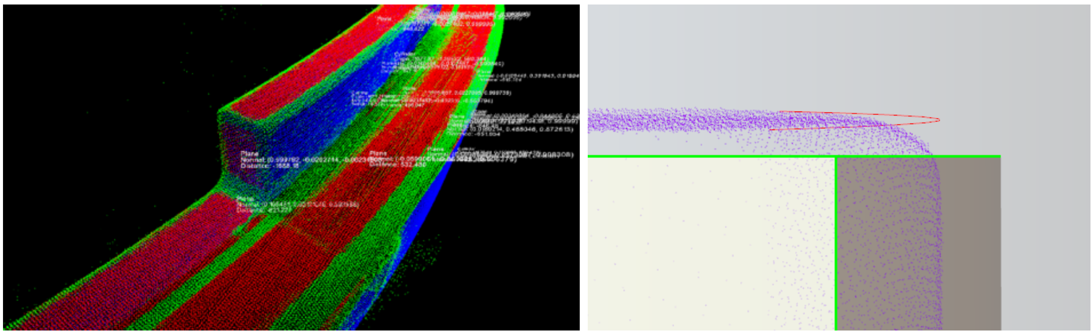

Figure 7: Left: RANSAC segmentation of the scans of one retaining lug. Cylindrical segments are blue, planes are red. Right: Calculated deburring path shown in red.

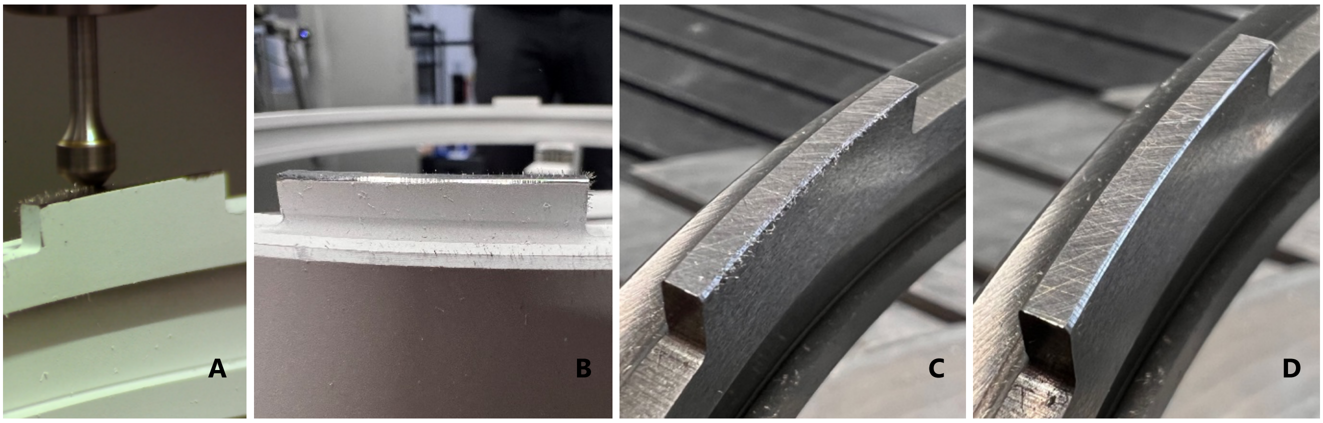

Figure 8: A: Deburring process. B: Resulting deburred edge. C: A second edge with chips and D: without chips.

## 4 Conclusion

In this paper, we presented our approach for adaptive robotic deburring of aerospace engine bearing rings based on data from two 3D sensors. We successfully employed our pipeline on edges of two retaining lugs. But needless to say, a lot of work remains to be done. A big challenge of bearing rings is their rotational symmetry and the almost featureless surface. When failing to properly align the scans used to plan the deburring path, even small deviations can lead to catastrophic outcomes like destroying a deburring tool, a workpiece or even the robot itself. A misaligned point cloud and the resulting destruction of the edge of a retaining lug is depicted in Figure 9. The misalignment occurs due to a lack of geometric features in some partial views. From the top view, for example, only flat areas are visible. This results in degrees of freedom during ICP Registration. Also, a quantitative analysis of the deburred edge needs to be carried out.

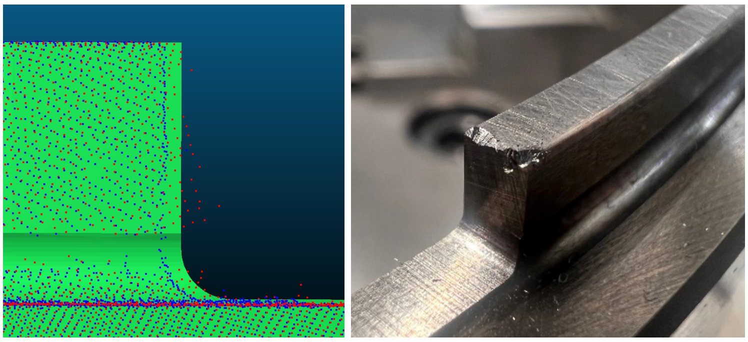

Figure 9: Left: Scans were not registered properly registered. Right: The deburring path was too close to the actual geometry, and the edge was destroyed.

## Acknowledgements

This research has been funded by the German Federal Ministry for Economic Affairs and Climate Action (BMWK) under the LuFo VI-2 program under grant no. 20D2113.

## References

[1] Z. Lai, R. Xiong, H. Wu and Y. Guan, “Integration of visual information and robot offline programming system for improving automatic deburring process,” *2018 IEEE international conference on robotics and biomimetics (ROBIO),* pp. 1132-1137, 2018.

[2] A. Kuss, M. Drust and A. Verl, “Detection of workpiece shape deviations for tool path adaptation in robotic deburring systems,” *Procedia CIRP,* vol. 57, pp. 545-550, 2016.

[3] H.-C. Song, B.-S. Kim and J.-B. Song, ”Tool path generation based on matching between teaching points and CAD model for robotic deburring,” *2012 IEEE/ASME International Conference on Advanced Intelligent Mechatronics (AIM),* pp. 890-895, 2012.

[4] S. Lloyd, R. A. Irani and M. Ahmadi, “Precision robotic deburring with Simultaneous Registration and Machining for improved accuracy, quality, and efficiency,” *Robotics and Computer-Integrated Manufacturing,* vol. 88, 2024.

[5] N. Andreff, H. Radu and E. Bernard, “On-line hand-eye calibration,” *Second International Conference on 3-D Digital Imaging and Modeling (Cat. No. PR00062),* pp. 430-436, 1999.

[6] I. A. Sucan, M. Moll, und L. E. Kavraki, „The Open Motion Planning Library“, *IEEE Robot. Automat. Mag.*, Bd. 19, Nr. 4, S. 72–82, Dez. 2012.

[7] J. D. Gammell, T. D. Barfoot, und S. S. Srinivasa, „Batch Informed Trees (BIT*): Informed Asymptotically Optimal Anytime Search“, *The International Journal of Robotics Research*, Bd. 39, Nr. 5, S. 543–567, Apr. 2020.

[8] E. Coumans und Y. Bai, „PyBullet, a Python module for physics simulation for games, robotics and machine learning“. 2021 2016. [Online]. Verfügbar unter: http://pybullet.org

[9] T. Rabbani, F. Van Den Heuvel and G. Vosselmann, “Segmentation of point clouds using smoothness constraint,” *International archives of photogrammetry, remote sensing and spatial information sciences,* vol. 36, no. 5, pp. 248-253, 2006.

[10] R. Schnabel, R. Wahl, und R. Klein, „Efficient RANSAC for Point-Cloud Shape Detection“, *Computer Graphics Forum*, Bd. 26, Nr. 2, S. 214–226, Juni 2007.